https://doi.org/10.5194/egusphere-2026-6629
Preprint. Discussion started: 30 October 2026
© Author(s) 2026. CC BY 4.0 License.

Emergent multiscale interdependence of land and ocean temperatures

Tommaso Alberti[1], Davide Faranda[2,3,4], and Valerio Lucarini[5,6]

[1]Istituto Nazionale di Geofisica e Vulcanologia, Rome, Italy
[2]Laboratoire des Sciences du Climat et de l'Environnement (LSCE/IPSL), CNRS, Université Paris-Saclay, Gif-sur-Yvette, France
[3]Laboratoire de Météorologie Dynamique (LMD/IPSL), École Normale Supérieure, École Polytechnique, PSL Research University, Paris, France
[4]London Mathematical Laboratory, London, UK
[5]University of Leicester, Leicester, UK
[6]Great Bay University, Dongguan, P.R. China

Correspondence: Tommaso Alberti (tommaso.alberti@ingv.it)

Abstract. Land and ocean temperatures share external forcing but respond through markedly different thermal memories. Using uncertainty-aware empirical mode decomposition and recurrence-based dynamical indicators, we show that sea-surface-temperature variability is systematically stretched toward longer periods relative to land-air temperature. This scale dilation is consistent with the increase in the ocean's effective heat capacity as progressively slower forcing penetrates to greater depths. Against this separated hierarchy, modern warming reorganizes the joint dynamics: the effective dimension decreases, recurrence persistence increases, and land–ocean co-recurrence strengthens. Synchronization first appears at multidecadal scales and its lower boundary subsequently contracts toward decadal and intermittent interannual scales. A concurrent increase in ocean evaporation, absent over land, further identifies the hydrological cycle and latent-energy exchange as a plausible pathway for this growing interdependence. Together, these diagnostics describe a scale-dependent reorganization associated with the warming background: land and ocean increasingly revisit similar configurations together, while the joint trajectory exhibits lower local dimension and greater recurrence persistence. Enhanced co-recurrence extends toward shorter timescales and exceeds a surrogate expectation that preserves the two warming backgrounds, although changes in observational coverage and quality remain a possible contributor.

1 Introduction

Interacting systems with contrasting response times need not react to common forcing by merely shifting their mean states. Their characteristic timescales may separate, the number of dynamically active degrees of freedom may contract, and initially distinct trajectories may become increasingly interdependent (Alberti et al., 2025). Detecting such changes from observations is difficult because forced non-stationarity coexists with internal variability, while conventional correlation measures contain little information about local geometry, persistence, or the scale dependence of the evolving dynamics (Lucarini et al., 2016a).

https://doi.org/10.5194/egusphere-2026-6629
Preprint. Discussion started: 30 October 2026
© Author(s) 2026. CC BY 4.0 License.

Scaling provides a complementary perspective on this multiscale organization. Schertzer and Lovejoy developed multiplicative-cascade descriptions of geophysical variability that connect scale invariance with intermittency and multifractal statistics (Schertzer and Lovejoy, 1987; Lovejoy and Schertzer, 2013). In the temporal domain, the distinction between weather, macroweather, and climate emphasizes that different ranges can exhibit different scaling behavior, rather than a single exponent applying across all timescales (Lovejoy et al., 2013). This motivates examining both the hierarchy of temperature fluctuations and how land–ocean interdependence varies across that hierarchy.

The land–ocean climate system provides a natural realization of this general problem. Land temperatures respond rapidly to radiative and atmospheric perturbations, whereas ocean heat capacity, vertical mixing, and circulation generate a much longer memory. This contrast explains the stronger mean warming over land (Sutton et al., 2007; Joshi et al., 2008), but its consequences extend beyond the mean response. The oceanic depth involved in thermal adjustment increases with the duration of the forcing, producing a scale-dependent effective heat capacity. At the same time, evaporation and latent-heat exchange connect the oceanic reservoir to the atmosphere and land, providing a possible pathway by which the initially separated thermal responses can become dynamically organized. Whether these processes leave an observable signature in the geometry and recurrence structure of global land and ocean temperatures remains unresolved.

Here we show that global land-air and sea-surface temperatures undergo a coherent multiscale reorganization. Their intrinsic modes form corresponding but nonidentical hierarchies, with ocean variability systematically shifted toward longer periods. The nonlinear temperature backgrounds subsequently diverge in amplitude while organizing the joint trajectory onto a lower-dimensional, more persistent manifold. Land–ocean co-recurrence first increases at multidecadal scales and later extends toward shorter periods. Finally, this transition is accompanied by a growing contrast between oceanic and terrestrial evaporation, consistent with an increasing role of ocean-supplied moisture and latent energy in the coupled dynamics.

2 Data and methods

2.1 Land and ocean temperature records and empirical mode decomposition

We analyze monthly global land-air temperature anomalies from CRUTEM5 (Osborn et al., 2021) and sea-surface-temperature anomalies from HadSST4.2 (Kennedy et al., 2019) over their common interval 1856–2026. Observational uncertainty is propagated through 500 realizations obtained by varying the raw data within their reported uncertainty ranges. Each realization is decomposed using empirical mode decomposition (EMD), which represents a nonstationary signal as a sum of data-adaptive intrinsic mode functions (IMFs) and a nonlinear residual (Huang et al., 1998; Wu and Huang, 2009),

$$T(t) = \sum_{k=1}^{K} c_k(t) + R(t). \tag{1}$$

The ensemble means of c_k and R define the analyzed components, while their ensemble spread quantifies sensitivity to observational uncertainty. The complete decompositions and sensitivity tests are reported in the Supplement.

https://doi.org/10.5194/egusphere-2026-6629
Preprint. Discussion started: 30 October 2026
© Author(s) 2026. CC BY 4.0 License.

2.2 Evaporation from the Twentieth Century Reanalysis

To examine a possible hydrological pathway, we additionally use monthly evaporation from the NOAA–CIRES–DOE Twentieth Century Reanalysis version 3 (20CRv3) (Slivinski et al., 2019, 2021). We use the individual 20CRv3 members to construct the evaporation ensemble, with separate area-weighted averages over land and ocean. This reanalysis ensemble is distinct from the 500 uncertainty realizations generated for the temperature records. The hydrological comparison is restricted to the overlap with the temperature analysis and is interpreted as a physical diagnostic test. Member-to-member variability does not, by itself, quantify systematic errors shared by the ensemble or establish the homogeneity of long-term evaporation trends.

3 Results

3.1 Separation of land and ocean timescales

Figure 1 shows the temperature records. Their amplitudes differ markedly, but both contain variability from subannual to centennial scales superimposed on accelerating backgrounds. The EMD modes reveal corresponding yet separated hierarchies (Fig. 2). Between the annual and multidecadal range,

$$\frac{P_k^{\mathrm{SST}}}{P_k^{\mathrm{L}}} > 1, \tag{2}$$

with ratios of approximately 1.2–1.9. A fit $P_k^{\mathrm{SST}} = a(P_k^{\mathrm{L}})^{\beta}$ gives $a = 1.17 \pm 0.08$ and $\beta = 1.10 \pm 0.05$, with uncertainty propagated from the observational ensemble. The longest components, whose nominal periods approach the record length, are not interpreted as stationary oscillations and are excluded from the inference of a universal scaling.

3.2 Power laws and scale-free properties

Within a finite range of scales, power-law spectra provide a second-order description of variability. They do not, by themselves, establish multifractality: multiplicative-cascade approaches also characterize how moments of different orders depend on scale (Schertzer and Lovejoy, 1987; Lovejoy and Schertzer, 2013). Fluctuation-based analyses, including Haar-wavelet methods, offer a complementary way to estimate scaling and identify changes between regimes (Lovejoy and Schertzer, 2012). Here we use spectral slopes and EMD periods to describe the observed hierarchy; we do not estimate a full multifractal spectrum. The slopes below should therefore be interpreted over their fitted frequency ranges, rather than as universal exponents spanning weather through climate (Lovejoy et al., 2013).

The power spectrum of atmospheric temperature follows a power law,

$$S_{\mathrm{atm}}(\omega) \propto \omega^{-\gamma}, \qquad \gamma = 1.4. \tag{3}$$

This scale-free structure explains why EMD produces a clean dyadic progression of IMF periods $P_k^L \approx 2^k\,\Delta t$: for a power-law spectrum, the EMD sifting algorithm acts as a dyadic filter bank, with each IMF capturing approximately one octave band (Wu

https://doi.org/10.5194/egusphere-2026-6629
Preprint. Discussion started: 30 October 2026
© Author(s) 2026. CC BY 4.0 License.

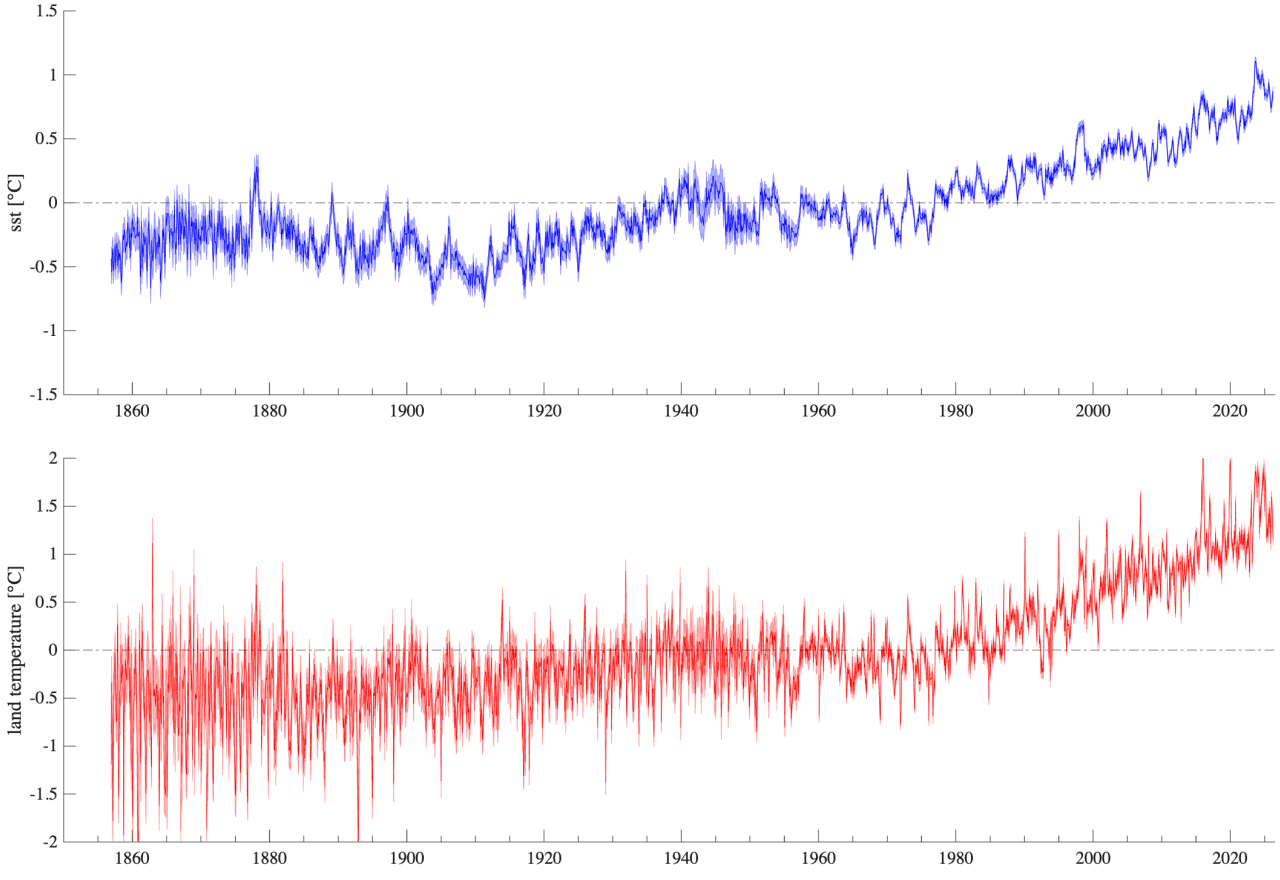

Figure 1. Monthly global land-air and sea-surface-temperature anomalies with observational uncertainty

and Huang, 2004; Flandrin et al., 2004). The power spectrum of SST also follows a power law,

$$S_{\mathrm{SST}}(\omega) \propto \omega^{-\delta}, \qquad \delta = 1.7, \tag{4}$$

with $\delta > \gamma$: the SST spectrum is redder than the atmospheric spectrum, consistent with $P_k^{\mathrm{SST}} > P_k^L$ at every mode k. Importantly, the difference

$$\delta - \gamma = 0.3 \tag{5}$$

is small, reflecting a modest but systematic reddening of the ocean spectrum relative to the atmosphere.

We can propose a single framework to explain the observations above. The ocean acts as a linear filter on the atmospheric forcing,

$$S_{\mathrm{SST}}(\omega) = |H(\omega)|^2 \, S_{\mathrm{atm}}(\omega), \tag{6}$$

https://doi.org/10.5194/egusphere-2026-6629
Preprint. Discussion started: 30 October 2026
© Author(s) 2026. CC BY 4.0 License.

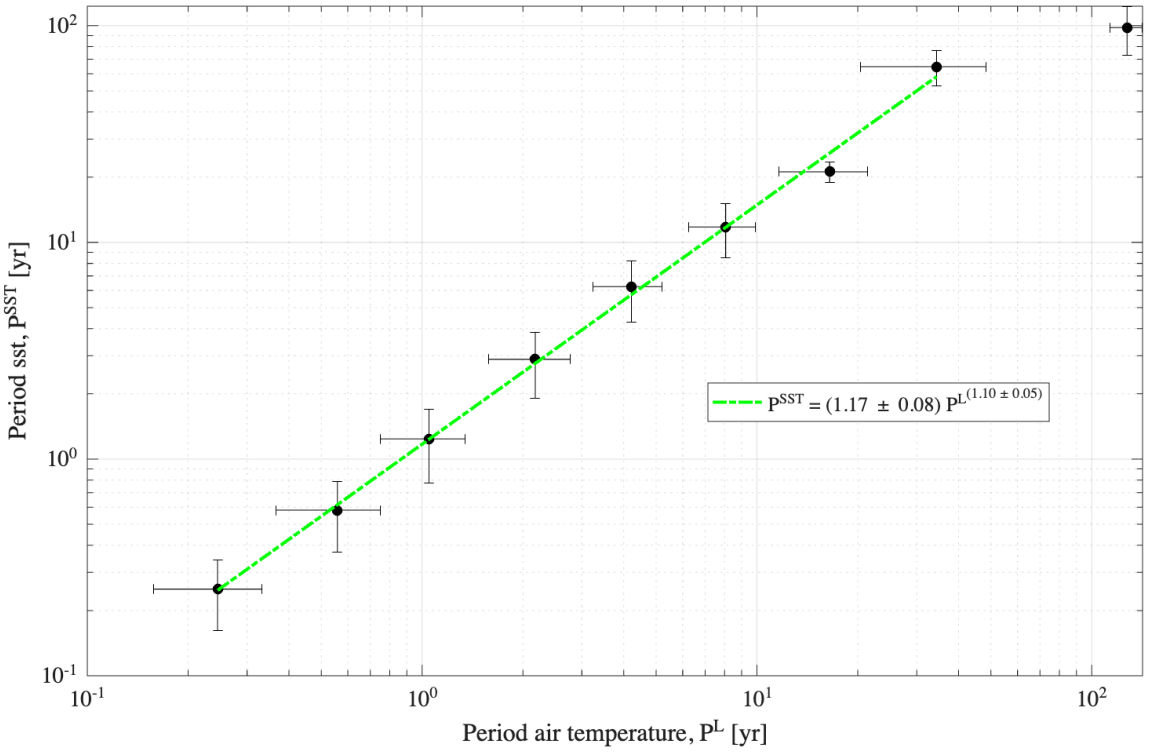

Figure 2. Characteristic periods of corresponding EMD modes. The dashed line marks equal periods; the solid line is the fit $P^{\mathrm{SST}} = a(P^{\mathrm{L}})^{\beta}$.

where $H(\omega)$ is the ocean transfer function. Substituting Eqs. (3) and (4) into Eq. (6) gives

$$|H(\omega)|^2 \propto \omega^{-(\delta-\gamma)} = \omega^{-0.3}, \tag{7}$$

a pure power law in frequency with no preferred scale, which is a direct consequence of both spectra being power laws.

A fractional integrator is one possible representation of this power-law gain. Scaling-based fractional stochastic models have been used to represent long memory in macroweather temperatures (Lovejoy et al., 2015). However, the ratio of power spectra constrains the gain, not the phase of the transfer function, and does not uniquely identify a causal land–ocean response. Under the additional fractional-integrator assumption, we write the transfer function $H(\omega) \propto (i\omega)^{-\nu}$. Identifying $2\nu = \delta - \gamma$ gives

$$\nu = \frac{\delta-\gamma}{2} = \frac{0.3}{2} = 0.15, \tag{8}$$

and the corresponding equation of motion is

$$\frac{d^{\nu}\mathrm{SST}(t)}{dt^{\nu}} \propto F_{\mathrm{atm}}(t) \quad \rightarrow \quad (i\omega)^{\nu}\widehat{\mathrm{SST}}(\omega) \propto \hat{F}_{\mathrm{atm}}(\omega), \tag{9}$$

where $\nu = 0.15$. The operator d^{ν}/dt^{ν} is the Riemann–Liouville fractional derivative of order ν, which interpolates between two limiting cases:

https://doi.org/10.5194/egusphere-2026-6629
Preprint. Discussion started: 30 October 2026
© Author(s) 2026. CC BY 4.0 License.

- $\nu = 1$, whereby Eq. (9) becomes $\dot{\mathrm{SST}} \propto F_{\mathrm{atm}}$, so that solving for SST requires integrating F_{atm} once.
- $\nu = 0$: the zeroth-order derivative is the identity operator, giving $\mathrm{SST} \propto F_{\mathrm{atm}}$, indicating instantaneous equilibration with no memory.

The observed $\nu = 0.15$, which is small, means the ocean is close to instantaneous equilibration but retains a slowly fading power-law memory of past forcing, consistent with the modest but systematic reddening $\delta - \gamma = 2\nu = 0.3$.

The following argument explores a possible link between the power-law filter and the EMD timescale scaling of Eq. (2). It is a heuristic construction, not a result established by the scaling references above.

The EMD sifting algorithm identifies the k-th IMF through the local extrema of the signal. The characteristic period of mode k is therefore controlled not by the energy in the dyadic band but by the *density of extrema* (zero-crossing rate) of the signal at that scale. For a stationary process with power-law spectrum $\omega^{-\alpha}$, the expected number of extrema per unit time, i.e. the Rice frequency, scales as the square root of the ratio of the second to the zeroth spectral moment:

$$\bar{\omega}^{(\alpha)} \propto \left(\frac{\int \omega^2 \omega^{-\alpha}\, d\omega}{\int \omega^{-\alpha}\, d\omega} \right)^{1/2}. \tag{10}$$

For a power-law spectrum truncated to the k-th dyadic band $[\omega_k, 2\omega_k]$, Eq. (10) gives

$$\bar{\omega}_k^{(\alpha)} = \omega_k\, f(\alpha), \qquad f(\alpha) = \left(\frac{(1-\alpha)(2^{3-\alpha}-1)}{(3-\alpha)(2^{1-\alpha}-1)} \right)^{1/2}, \tag{11}$$

where $f(\alpha)$ depends only on the spectral slope, not on k. Within a fixed dyadic band the ratio $f(\delta)/f(\gamma)$ is constant across modes, which would give $\beta = 1$. The key is that the *band boundaries themselves* are not fixed: they are determined by the extrema density of the full signal. For a power-law spectrum $\omega^{-\alpha}$ over the full frequency range $[\omega_{\min}, \omega_{\max}]$, the cumulative extrema density up to frequency ω scales as $\omega^{(3-\alpha)/2}$. The EMD sifting algorithm extracts modes in order of decreasing frequency, so the k-th mode boundary $\omega_k^{(\alpha)}$ is set by the condition that the first k modes account for a fixed fraction of the total extrema:

$$\left(\frac{\omega_k^{(\alpha)}}{\omega_{\max}} \right)^{(3-\alpha)/2} = \frac{K-k}{K}, \tag{12}$$

giving

$$\omega_k^{(\alpha)} \propto \left(\frac{K-k}{K} \right)^{2/(3-\alpha)}. \tag{13}$$

Pairing mode k of the atmosphere ($\alpha = \gamma$) with mode k of the ocean ($\alpha = \delta$) and eliminating k yields

$$\Omega_k^{\mathrm{SST}} \propto \left(\omega_k^L\right)^{(3-\gamma)/(3-\delta)}, \tag{14}$$

and converting to periods $P = 2\pi/\omega$:

$$P_k^{\mathrm{SST}} = \alpha \left(P_k^L\right)^{\beta}, \qquad \beta = \frac{3-\gamma}{3-\delta}. \tag{15}$$

https://doi.org/10.5194/egusphere-2026-6629
Preprint. Discussion started: 30 October 2026
© Author(s) 2026. CC BY 4.0 License.

With $\gamma = 1.4$ and $\delta = 1.7$:

$$\beta = \frac{3-1.4}{3-1.7} = \frac{1.6}{1.3} \approx 1.23. \tag{16}$$

This is close to, but not exactly equal to, the observed $\beta = 1.10 \pm 0.05$. The residual discrepancy is consistent with two known limitations of the theoretical argument: first, the EMD sifting algorithm is not a perfect zero-crossing counter and its effective spectral moment lies between the zeroth and second moments; second, the actual power spectra deviate from perfect power laws at finite record length, introducing higher-order corrections to the extrema density scaling. Within these caveats, $\beta \approx (3-\gamma)/(3-\delta)$ provides a parameter-free prediction of the EMD timescale scaling exponent from the independently measured spectral slopes γ and δ.

3.3 Physical interpretation via a scale-dependent heat capacity

The fractional integrator has a direct physical interpretation. Returning to the standard derivative, we assume that the SST field has a timescale-dependent heat capacity C_{eff}. In Fourier space, one obtains:

$$i\omega C_{\text{eff}}(\omega)\,\widehat{\text{SST}}(\omega) \propto \hat{F}_{\text{atm}}(\omega). \tag{17}$$

Matching this to Eq. (9), one obtains that $C_{\text{eff}}(\omega) \propto \omega^{-(1-\nu)} = \omega^{-0.85}$. This means that the effective heat capacity increases at lower frequencies.

Now compare with classical Fickian diffusion. For a periodic surface forcing at frequency ω, the thermal penetration depth scales as $h_{\text{diff}}(\omega) \propto \omega^{-1/2}$, which, since $C_{\text{eff}}(\omega) \propto h_{\text{diff}}(\omega)$ gives $C_{\text{eff}}(\omega) \propto \omega^{-1/2}$. The observed exponent is $0.85 > 0.5$. This means that the heat capacity grows faster with period than classical diffusion predicts, so that deeper layers are entrained more efficiently than simple diffusion would suggest. Such an anomalous hyper-diffusive entrainment aligns well with the KPP parametrization (Large et al., 1994) and results from a combination of advective-diffusive mechanisms, including wind-driven mixing and Ekman pumping, mesoscale eddies, and, especially, the large-scale ocean circulation.

3.4 Nonlinear land and ocean temperature backgrounds

The nonlinear residuals clarify how the two slow responses subsequently evolve (Fig. 3). Land and ocean follow a common curved trajectory, but the land residual accelerates more rapidly and increasingly departs from the ocean residual during recent warming. In the parametric representation $R^{\text{SST}}(t)$ versus $R^{\text{L}}(t)$, the trajectory bends below the equal-response line, directly displaying the attenuation of the oceanic surface response. The common zero crossing near 1968 depends on the anomaly reference and is not interpreted as a physical transition; the robust feature is the growing separation and curvature of the two residuals.

3.5 Recurrence-based dynamical indicators

To determine whether this scale separation accompanies a change in dynamical organization, we use recurrence-based indicators derived from extreme-value statistics (Lucarini et al., 2016b; Faranda et al., 2017; Alberti et al., 2025). For a trajectory

https://doi.org/10.5194/egusphere-2026-6629
Preprint. Discussion started: 30 October 2026
© Author(s) 2026. CC BY 4.0 License.

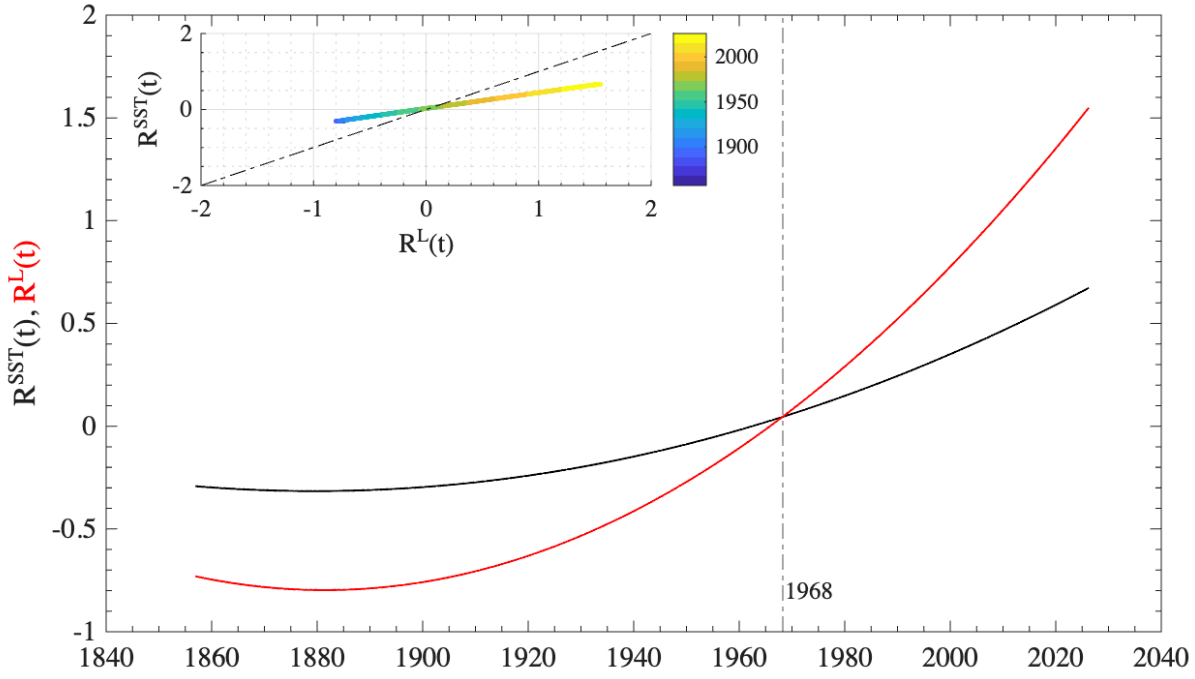

Figure 3. Nonlinear land and ocean temperature backgrounds. The main panel shows the EMD residuals $R^{\mathrm{L}}(t)$ and $R^{\mathrm{SST}}(t)$. The inset gives their parametric trajectory, colored by year; the dashed diagonal denotes equal land and ocean responses. The increasing departure below the diagonal reflects the attenuated and delayed oceanic surface response relative to land.

in the joint land–ocean state space, recurrences near the state occupied at time t define three instantaneous quantities. The dimension $d(t)$ estimates the local number of active degrees of freedom. The extremal index $0 \leq \theta(t) \leq 1$ measures recurrence clustering: small values denote long residence and high persistence, whereas values near unity indicate rapid departure. The co-recurrence ratio $0 \leq \alpha(t) \leq 1$ measures the fraction of simultaneous land and ocean recurrences and therefore their instantaneous dynamical interdependence. These indicators describe complementary geometric and temporal properties without assuming linear dependence or stationarity.

We first apply the indicators to the original records and to counterparts from which the EMD residuals have been removed. Figure 4 shows that retaining the residuals systematically reduces d, particularly near the beginning of the record and after the mid-twentieth century. The trajectory with the warming background retained therefore has a lower estimated local dimension than its detrended counterpart, reminiscent of the hammam effect discussed by Faranda et al. (2019). Here, dimension characterizes the local recurrence geometry of the analyzed temperature variables; it is neither a measure of thermodynamic entropy nor an estimate of the total number of microscopic degrees of freedom of the climate system. The decrease in d is consistent

https://doi.org/10.5194/egusphere-2026-6629
Preprint. Discussion started: 30 October 2026
© Author(s) 2026. CC BY 4.0 License.

with a dominant common direction associated with the slow components and does not imply a decrease in thermodynamic entropy or greater thermodynamic stability.

The extremal index provides a separate temporal diagnostic. Values of θ are generally lower when the residuals are retained, indicating longer persistence of dynamically similar configurations. This empirical behavior is not a consequence of the decrease in d: local dimension and recurrence clustering describe distinct properties and need not vary together. The most pronounced change occurs in α. Detrended temperatures remain weakly to moderately interdependent, with intermittent co-recurrence episodes. In the original records, α increases sharply around the middle of the twentieth century and remains elevated thereafter, reaching values near 0.6. For these records, the observed combination of changes is summarized by

$$d\downarrow, \qquad \theta\downarrow, \qquad \alpha\uparrow. \tag{18}$$

Scaling-based tests of climatic change stress the need to account for long-range dependence when constructing a natural-variability null hypothesis (Lovejoy, 2014). Here the surrogate test addresses a narrower question: whether the retained warming backgrounds, combined with independently resampled oscillatory components, reproduce the observed co-recurrence. Its validity depends on how well the resampling preserves the relevant temporal dependence.

A common-trend surrogate test preserves both observed nonlinear residuals while independently block-resampling the oscillatory IMF coordinates of land and ocean. The observed interdependence increasingly exceeds this null expectation after the mid-twentieth century, particularly at decadal and multidecadal scales (Fig. S3 in the Supplement). Within this surrogate framework, preserving the two smooth warming backgrounds alone does not reproduce the observed interdependence. However, the test does not isolate the effects of evolving observational coverage, measurement practices, or reconstruction uncertainty. Improvements in data quality could contribute to the apparent increase in co-recurrence, particularly when comparing the sparsely observed early record with recent decades. Propagating the reported temperature uncertainties addresses sensitivity to those uncertainty estimates, but does not establish that all time-dependent observational effects have been removed. Distinguishing a physical change from these effects requires additional tests using coverage-matched records, a common sampling mask, and alternative temperature products; these tests are not provided here.

3.6 Multiscale dynamical reorganization

The one-dimensional comparison does not identify the scales at which this reorganization develops. At multiscale level m, we therefore treat the first m IMFs as coordinates of the land and ocean state vectors,

$$\mathbf{x}_m(t) = \left[c_1^{\mathrm{L}}(t), \ldots, c_m^{\mathrm{L}}(t)\right], \tag{19}$$

$$\mathbf{y}_m(t) = \left[c_1^{\mathrm{SST}}(t), \ldots, c_m^{\mathrm{SST}}(t)\right], \tag{20}$$

ordered from fast to slow variability, with the residual included as the final coordinate. The components are not summed into scalar cumulative reconstructions. Applying the recurrence analysis at every m yields $d(t,\tau)$, $\theta(t,\tau)$, and $\alpha(t,\tau)$, where τ is the characteristic period of the slowest coordinate admitted at that level (Alberti et al., 2023b, a).

https://doi.org/10.5194/egusphere-2026-6629
Preprint. Discussion started: 30 October 2026
© Author(s) 2026. CC BY 4.0 License.

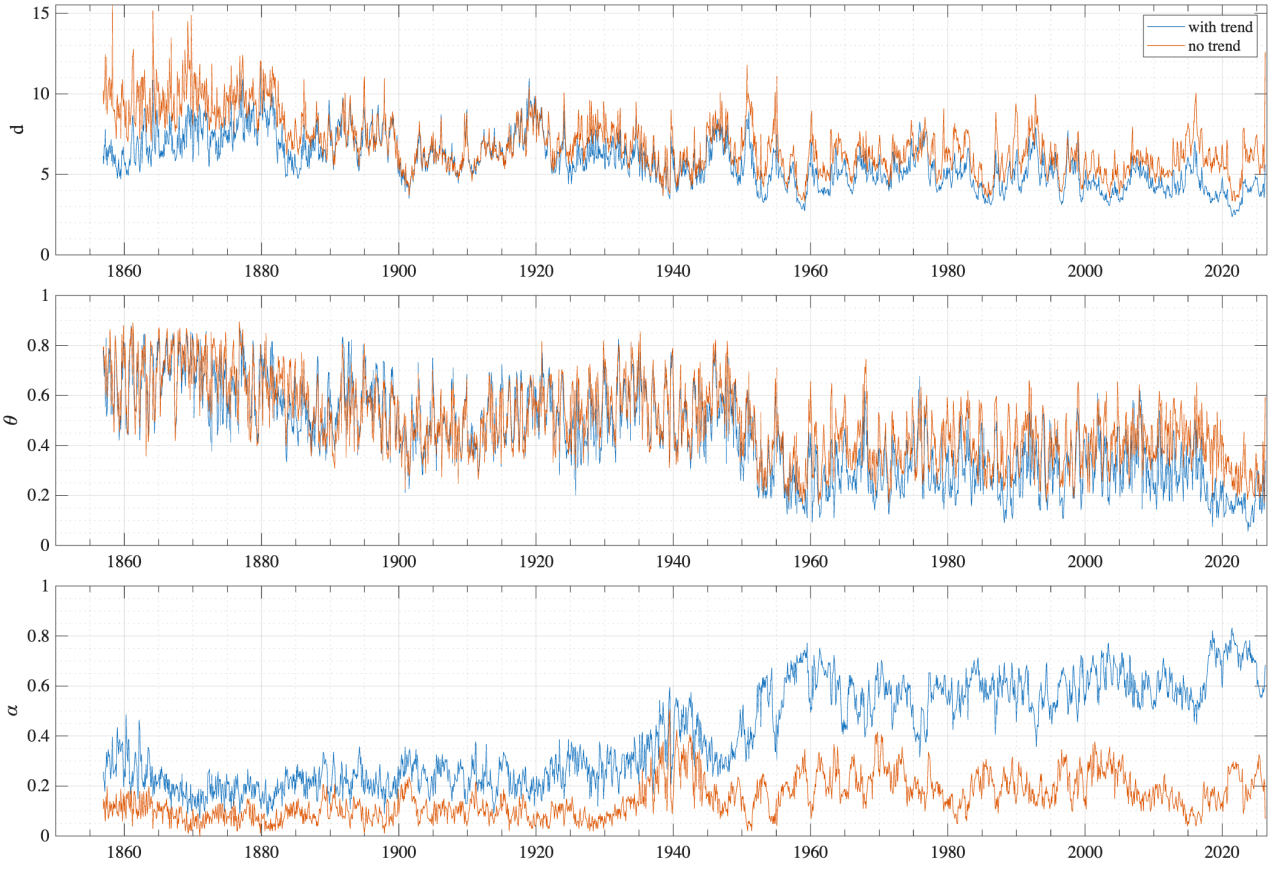

Figure 4. Joint land–ocean recurrence diagnostics with and without the warming background. Instantaneous dimension d (top), extremal index θ (center), and co-recurrence ratio α (bottom) computed from the original records (blue) and their detrended oscillatory components (orange). Lower d denotes a lower-dimensional neighborhood, lower θ greater persistence, and larger α stronger dynamical interdependence.

Figure 5 shows that the scale of maximum local dimension is not fixed. High dimensionality initially occupies a broad range of periods, whereas the modern interval has a lower background dimension interrupted by episodic bands of enhanced complexity. Persistence predictably increases toward slower components, but it also expands temporally: in recent decades, low-$\theta(t,\tau)$ conditions reach periods shorter than those affected earlier in the record.

The co-recurrence map provides the clearest signature. Before the twentieth century, $\alpha(t,\tau)$ is small over most scales. Enhanced interdependence first appears in the multidecadal-to-centennial components around 1940. After the mid-twentieth century, the high-α region broadens and its lower boundary progressively contracts from multidecadal toward decadal and, intermittently, interannual periods. We refer to this downward migration as a contraction of the characteristic synchronization timescale: progressively faster components enter the coherent regime. Here "synchronization cascade" describes the observed

https://doi.org/10.5194/egusphere-2026-6629
Preprint. Discussion started: 30 October 2026
© Author(s) 2026. CC BY 4.0 License.

progression of enhanced co-recurrence across scales. It does not establish a multiplicative transfer process of the kind modeled in multifractal cascade theory (Schertzer and Lovejoy, 1987; Lovejoy and Schertzer, 2013).

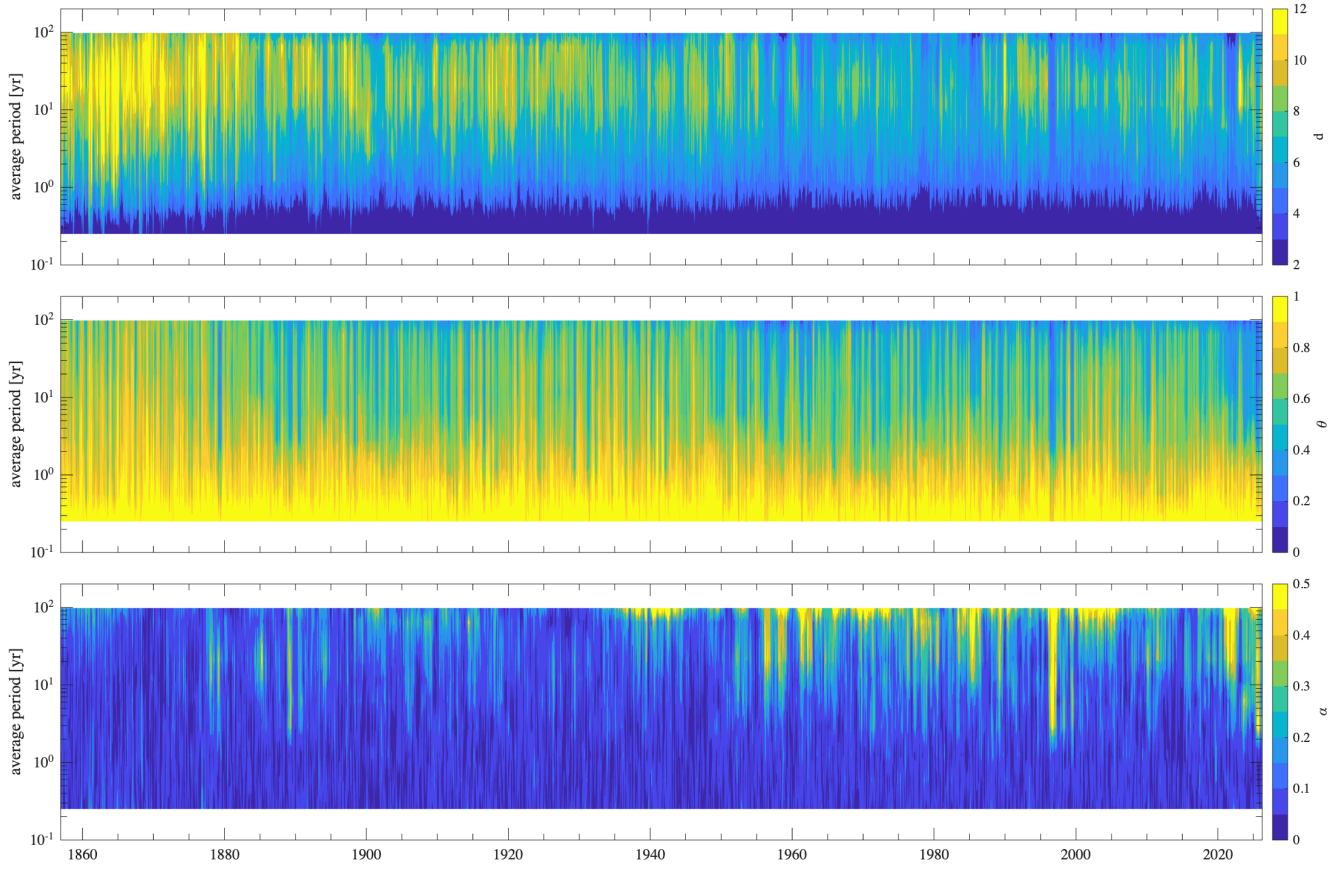

Figure 5. Multiscale dynamical reorganization of global land and ocean temperatures. From top to bottom: instantaneous dimension $d(t,\tau)$, extremal index $\theta(t,\tau)$, and co-recurrence ratio $\alpha(t,\tau)$ obtained by progressively augmenting the state vectors with slower IMF coordinates. The lower boundary of enhanced α moves toward shorter periods during the modern interval.

3.7 A possible hydrological pathway

The hydrological cycle provides a plausible physical pathway for this reorganization. Evaporation transfers both moisture and latent energy from the surface to the atmosphere. Over the ocean, water supply is effectively unlimited and evaporation can increase as the surface warms and the near-surface humidity gradient and turbulent exchange change. Over land, evaporation is additionally constrained by soil-moisture availability, vegetation, and surface resistance. Consequently, the two components need not evolve proportionally under warming.

https://doi.org/10.5194/egusphere-2026-6629
Preprint. Discussion started: 30 October 2026
© Author(s) 2026. CC BY 4.0 License.

This contrast is visible in 20CRv3 (Fig. 6). The global land-average evaporation retains a strong seasonal cycle but shows little comparable secular change, whereas ocean-average evaporation exhibits a pronounced increase. The ocean–land evaporation contrast

$$\Delta E(t) = E_{\mathrm{ocean}}(t) - E_{\mathrm{land}}(t) \tag{21}$$

therefore grows during the same broad interval in which multidecadal $\alpha(t, \tau)$ strengthens and its lower boundary moves toward shorter periods. This correspondence is physically consistent with a larger oceanic supply of moisture and latent energy to the atmosphere, which can communicate ocean thermal anomalies to the atmosphere and land while land-surface moisture limitations regulate the return flux. More generally, an intensified hydrological cycle can alter salinity, stratification, and ocean heat uptake, thereby feeding back on the thermal memory of the coupled system (Liu et al., 2021).

The evaporation hypothesis must be interpreted carefully. Co-evolution does not establish mediation, and long-term hydrological trends in a reanalysis are less directly constrained than temperature observations, particularly early in the record. The result is therefore used to identify a testable mechanism rather than to claim that evaporation alone causes the increase in α. A decisive test would require independent flux products over their common period and a conditional recurrence analysis asking whether land–ocean temperature interdependence decreases after conditioning on oceanic evaporation, latent-heat flux, and atmospheric moisture transport.

4 Discussion

These findings suggest a physical interpretation linking contrasting thermal memories to the observed recurrence structure. The longer SST timescales are consistent with greater oceanic thermal inertia. Retaining the nonlinear warming backgrounds is associated with lower local dimension and greater recurrence persistence, while enhanced land–ocean co-recurrence appears first at slow scales and subsequently extends toward shorter periods. The evaporation contrast motivates moisture and latent-energy exchange as a candidate mechanism linking the subsystems. This interpretation remains a hypothesis: the present diagnostics do not establish a causal sequence from warming through evaporation to enhanced interdependence, and observational inhomogeneity remains a possible contributor.

Our interpretation remains dynamical rather than directional. Co-recurrence does not determine whether land drives ocean, ocean drives land, or both respond through atmosphere–ocean feedbacks and external forcing. The empirical result is that the analyzed records exhibit concurrent, scale-dependent changes in geometry, persistence, and co-recurrence; establishing their robustness to observational inhomogeneity requires the additional tests outlined above. This differs from a conventional increase in correlation: the transition combines timescale dilation between the subsystems, contraction of the effective dimension, increased persistence, and a synchronization boundary moving toward shorter periods.

This reorganization may also matter for climate extremes. Long-lived ocean-temperature anomalies maintain anomalous surface fluxes and atmospheric moisture, while rapidly warming land surfaces amplify near-surface temperature departures. A regime in which the two components recur more persistently and coherently may therefore provide a dynamical background

https://doi.org/10.5194/egusphere-2026-6629
Preprint. Discussion started: 30 October 2026
© Author(s) 2026. CC BY 4.0 License.

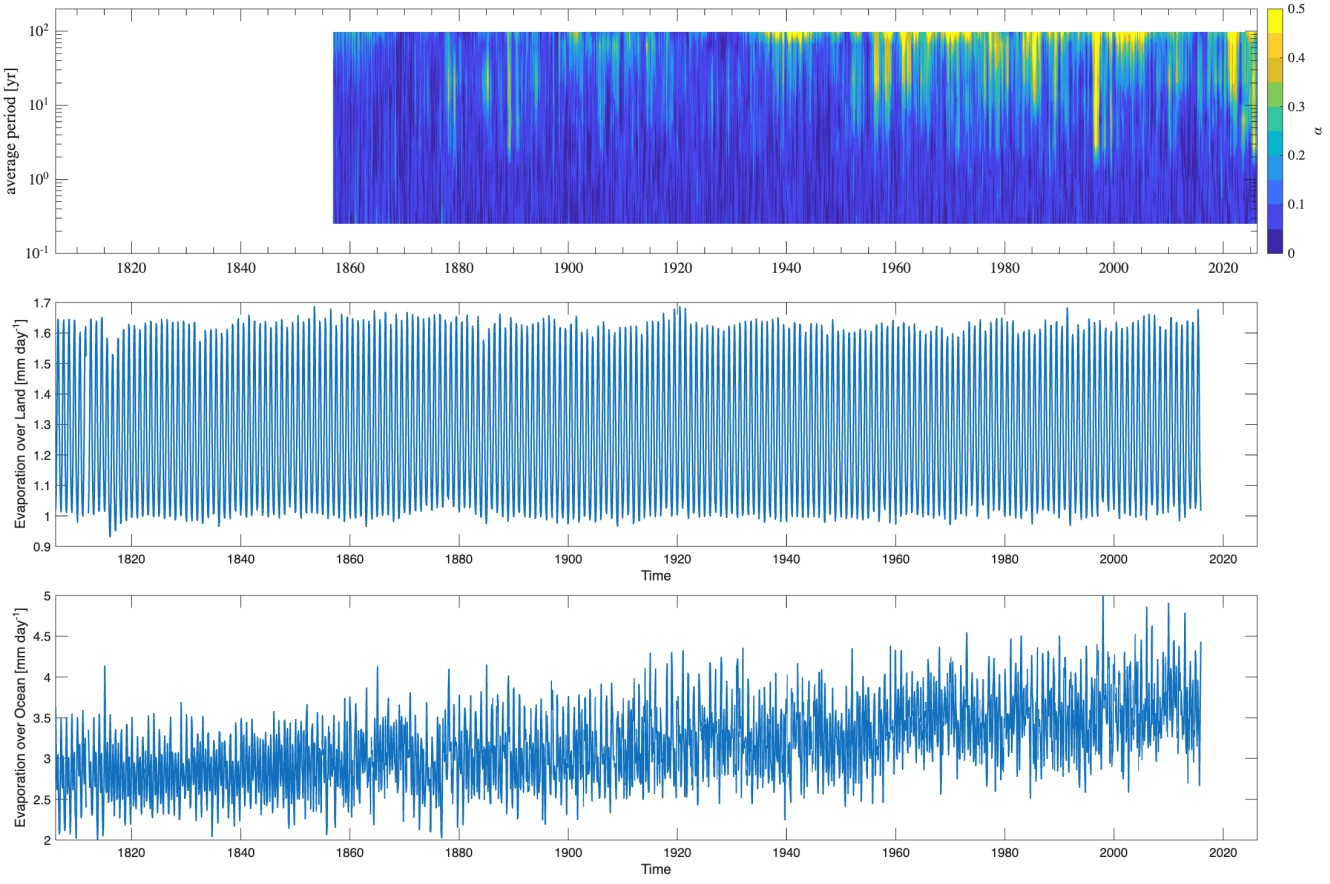

Figure 6. Hydrological context of the land–ocean dynamical reorganization. Top: temperature co-recurrence ratio $\alpha(t, \tau)$ as in Fig. 5. Middle and bottom: global area-weighted evaporation over land and ocean, respectively, from 20CRv3. Ocean evaporation increases over the historical record, while land evaporation exhibits no comparable secular rise. The temporal correspondence with enhanced multidecadal α identifies latent-energy and moisture exchange as a candidate pathway, not as a causal attribution.

favorable to prolonged or compound land–ocean heat anomalies. Our global-mean analysis neither attributes individual heat waves or marine heat waves nor identifies a regional mechanism. It instead motivates spatially resolved and event-based tests of whether the observed multiscale reorganization affects their persistence and co-occurrence.

5 Conclusions

More broadly, the combination of multiscale decomposition and recurrence diagnostics offers a framework for investigating coupled systems with contrasting memory times. In the land–ocean records examined here, it resolves differences in charac-

https://doi.org/10.5194/egusphere-2026-6629
Preprint. Discussion started: 30 October 2026
© Author(s) 2026. CC BY 4.0 License.

teristic periods alongside changes in local geometry, persistence, and co-recurrence. Whether similar patterns occur in other systems, and which mechanisms generate them, remains to be tested with controlled models and independent observations.

Code and data availability. CRUTEM5 land-air temperature anomalies (Osborn et al., 2021) and HadSST4.2 sea-surface-temperature anomalies (Kennedy et al., 2019) are publicly available from the Met Office Hadley Centre and the Climatic Research Unit. Evaporation from the NOAA–CIRES–DOE Twentieth Century Reanalysis version 3 (Slivinski et al., 2019, 2021) is publicly available from NOAA PSL.

Author contributions. TA conceived the study and performed the analysis. TA, DF, and VL interpreted the results and wrote the manuscript.

Competing interests. The authors declare that they have no conflict of interest.

Acknowledgements. This research received funding from Ministero dell'Università e della Ricerca under the call Fondo Italiano per la Scienza 2022–2023 (FIS-2) for the project "Mediterranean Extreme Events and Tipping elements in a changing climate on multiple spatiotemporal scales", grant number FIS-2023-00159, CUP: D53C24005450001. VL gratefully acknowledge funding received from the European Space Agency (ESA) for the PREDICT project (contract no. 4000146344/24/I-LR) and from the Advanced Research and Invention Agency (ARIA) for the AdvanTip project (grant no. SCOP-PR01-P003). VL also acknowledges the partial support provided by the Horizon Europe Projects Past2Future (Grant No. 101184070) and ClimTIP (Grant No. 100018693), by the NNSFC International Collaboration Fund for Creative Research Teams (Grant No. W2541005), and the support received as Simons Fellow of the I. Newton Institute, Cambridge (FCPW01 programme).

https://doi.org/10.5194/egusphere-2026-6629
Preprint. Discussion started: 30 October 2026
© Author(s) 2026. CC BY 4.0 License.

References

Alberti, T., Daviaud, F., Donner, R. V., Dubrulle, B., Faranda, D., and Lucarini, V.: Chameleon attractors in turbulent flows, Chaos Solitons and Fractals, 168, 113195, https://doi.org/10.1016/j.chaos.2023.113195, 2023a.

Alberti, T., Faranda, D., Lucarini, V., Donner, R. V., Dubrulle, B., and Daviaud, F.: Scale dependence of fractal dimension in deterministic and stochastic Lorenz-63 systems, Chaos, 33, 023144, https://doi.org/10.1063/5.0106053, 2023b.

Alberti, T., Florindo, F., Rohling, E. J., Lucarini, V., and Faranda, D.: Contrasting dynamics of past climate states and critical transitions via dimensional analysis, Sci. Rep., 15, 13 224, https://doi.org/10.1038/s41598-025-96432-6, 2025.

Faranda, D., Messori, G., and Yiou, P.: Dynamical proxies of North Atlantic predictability and extremes, Sci. Rep., 7, 41 278, https://doi.org/10.1038/srep41278, 2017.

Faranda, D., Alvarez-Castro, M. C., Messori, G., Rodrigues, D., and Yiou, P.: The hammam effect or how a warm ocean enhances large scale atmospheric predictability, Nature communications, 10, 1–7, 2019.

Flandrin, P., Rilling, G., and Gonçalvès, P.: Empirical mode decomposition as a filter bank, IEEE Signal Processing Letters, 11, 112–114, https://doi.org/10.1109/LSP.2003.821662, 2004.

Huang, N. E., Shen, Z., Long, S. R., Wu, M. C., Shih, H. H., Zheng, Q., Yen, N.-C., Tung, C. C., and Liu, H. H.: The empirical mode decomposition and the Hilbert spectrum for nonlinear and non-stationary time series analysis, Proc. R. Soc. Lond. A, 454, 903–995, https://doi.org/10.1098/rspa.1998.0193, 1998.

Joshi, M. M., Gregory, J. M., Webb, M. J., Sexton, D. M. H., and Johns, T. C.: Mechanisms for the land/sea warming contrast exhibited by simulations of climate change, Clim. Dyn., 30, 455–465, https://doi.org/10.1007/s00382-007-0306-1, 2008.

Kennedy, J. J., Rayner, N. A., Atkinson, C. P., and Killick, R. E.: An ensemble data set of sea-surface temperature change from 1850: The Met Office Hadley Centre HadSST.4.0.0.0 data set, J. Geophys. Res. Atmos., 124, 7719–7763, https://doi.org/10.1029/2018JD029867, 2019.

Large, W. G., McWilliams, J. C., and Doney, S. C.: Oceanic vertical mixing: A review and a model with a nonlocal boundary layer parameterization, Reviews of Geophysics, 32, 363–403, https://doi.org/https://doi.org/10.1029/94RG01872, 1994.

Liu, M., Vecchi, G. A., Soden, B. J., et al.: Enhanced Hydrological Cycle Increases Ocean Heat Uptake and Moderates Transient Climate Change, Nature Climate Change, 11, 848–853, https://doi.org/10.1038/s41558-021-01152-0, 2021.

Lovejoy, S.: Scaling fluctuation analysis and statistical hypothesis testing of anthropogenic warming, Climate Dynamics, 42, 2339–2351, https://doi.org/10.1007/s00382-014-2128-2, 2014.

Lovejoy, S. and Schertzer, D.: Haar wavelets, fluctuations and structure functions: convenient choices for geophysics, Nonlinear Processes in Geophysics, 19, 513–527, https://doi.org/10.5194/npg-19-513-2012, 2012.

Lovejoy, S. and Schertzer, D.: The Weather and Climate: Emergent Laws and Multifractal Cascades, Cambridge University Press, https://doi.org/10.1017/CBO9781139093811, 2013.

Lovejoy, S., Schertzer, D., and Varon, D.: Do GCMs predict the climate ... or macroweather?, Earth System Dynamics, 4, 439–454, https://doi.org/10.5194/esd-4-439-2013, 2013.

Lovejoy, S., del Rio Amador, L., and Hébert, R.: The ScaLIng Macroweather Model (SLIMM): using scaling to forecast global-scale macroweather from months to decades, Earth System Dynamics, 6, 637–658, https://doi.org/10.5194/esd-6-637-2015, 2015.

Lucarini, V., Faranda, D., de Freitas, A. C. G. M. M., de Freitas, J. M. M., Holland, M., Kuna, T., Nicol, M., Todd, M., and Vaienti, S.: Extremes and Recurrence in Dynamical Systems, Wiley, New York, 2016a.

https://doi.org/10.5194/egusphere-2026-6629
Preprint. Discussion started: 30 October 2026
© Author(s) 2026. CC BY 4.0 License.

Lucarini, V., Faranda, D., Freitas, A. C. M., Freitas, J. M., Holland, M., Kuna, T., Nicol, M., Todd, M., and Vaienti, S.: Extremes and Recurrence in Dynamical Systems, Wiley, Hoboken, ISBN 9781118632192, 2016b.

Osborn, T. J., Jones, P. D., Lister, D. H., Morice, C. P., Simpson, I. R., Winn, J. P., Hogan, E., and Harris, I. C.: Land surface air temperature variations across the globe updated to 2019: The CRUTEM5 data set, J. Geophys. Res. Atmos., 126, e2019JD032 352, https://doi.org/10.1029/2019JD032352, 2021.

Schertzer, D. and Lovejoy, S.: Physical modeling and analysis of rain and clouds by anisotropic scaling multiplicative processes, Journal of Geophysical Research: Atmospheres, 92, 9693–9714, https://doi.org/10.1029/JD092iD08p09693, 1987.

Slivinski, L. C. et al.: Towards a More Reliable Historical Reanalysis: Improvements for Version 3 of the Twentieth Century Reanalysis System, Quarterly Journal of the Royal Meteorological Society, 145, 2876–2908, https://doi.org/10.1002/qj.3598, 2019.

Slivinski, L. C. et al.: An Evaluation of the Performance of the Twentieth Century Reanalysis Version 3, Journal of Climate, 34, 1417–1438, https://doi.org/10.1175/JCLI-D-20-0505.1, 2021.

Sutton, R. T., Dong, B., and Gregory, J. M.: Land/sea warming ratio in response to climate change: IPCC AR4 model results and comparison with observations, Geophys. Res. Lett., 34, L02 701, https://doi.org/10.1029/2006GL028164, 2007.

Wu, Z. and Huang, N. E.: A study of the characteristics of white noise using the empirical mode decomposition method, Proceedings of the Royal Society of London. Series A: Mathematical, Physical and Engineering Sciences, 460, 1597–1611, https://doi.org/10.1098/rspa.2003.1221, 2004.

Wu, Z. and Huang, N. E.: Ensemble empirical mode decomposition: A noise-assisted data analysis method, Adv. Adapt. Data Anal., 1, 1–41, https://doi.org/10.1142/S1793536909000047, 2009.